1 **Increased Grounding Zone Ice Flux and Dynamic Thinning Creates Vulnerable Regions on**

2 **George VI Ice Shelf, Antarctic Peninsula**

4 Indrani Das[1*], Jowan M. Barnes[2], James A. Smith[3], Renata R. Constantino[1,4], Sidney R.

5 Hemming[5], Laurie Padman[6]

6 *Corresponding author: indrani@ldeo.columbia.edu

8 1. Lamont-Doherty Earth Observatory, Columbia University, NY, USA

9 2. Northumbria University, Newcastle upon Tyne, UK

10 3. British Antarctic Survey, Cambridge, UK

11 4. Institute of Astronomy, Geophysics and Atmospheric Sciences, University of São Paulo,

12 Brazil

13 5. Department of Earth and Environmental Sciences, Columbia University, NY

14 6. Earth and Space Research, OR, USA

24 **Abstract.** George VI Ice Shelf (GVIIS), on the western side of the Antarctic Peninsula, is

25 currently losing mass. Paleo observations suggest that atmospheric and oceanic warming in the

26 early Holocene caused complete loss of the ice shelf, leading to the possibility that modern

27 observed warming can initiate a similar loss. Ice shelf loss is assumed to be, primarily, a direct

28 response to atmospheric and ocean warming through increased hydrofracture and basal melting.

29 Here, however, we consider the hypothesis that increased lubrication of grounded ice is a further

30 contributor to destabilizing the ice shelf, where the lubrication may come from processes such as

31 increased surface meltwater percolating to the base of glaciers or changes in liquid water fluxes

32 across the grounding line. Motivated by the differences in our observation-based strain-induced

33 dynamic thickness change between 2013–2018 along the northern and southern sectors GVIIS

34 which also experiences variable surface melt, we use an ice sheet model to investigate this

35 hypothesis. We find that, as expected, reduced bed friction increases the flow of grounded ice.

36 However, because of the unique ice flow and buttressing features of GVIIS, the increased ice

37 flux across the grounding line also increases compression of the northern GVIIS, which makes it

38 resistant to rifting and hydrofracture. In contrast, the southern GVIIS, which is fed by ice streams

39 sitting on submarine beds, experiences continued divergence. We suggest that the associated

40 strain thinning reduces buttressing of grounded ice, creating a positive feedback of accelerated

41 ice inflow to the southern GVIIS and likely making it more vulnerable to future retreats than the

42 northern sector.

43

44 **Plain language summary.** George VI Ice Shelf (GVIIS) on the western Antarctic Peninsula is

45 currently thinning and the glaciers feeding the ice shelf are accelerating. Geologic evidence

46 indicates that GVIIS had previously disappeared several thousand years ago as regional air and

47   ocean temperatures increased, similar to what the region is experiencing now. In this work, we

48   use remote sensing and numerical modeling to show that the southern side is likely more

49   vulnerable because of ice dynamics and thinning triggered by increased ice velocity and ice flux,

50   in contrast to paleo observations that proposed that the past retreat proceeded from the north.

51

52   **1. Introduction**

53   The glaciers draining the Antarctic Peninsula (AP) have undergone widespread retreat and

54   acceleration during recent decades (Pritchard et al., 2009; Scambos et al., 2009; Rignot et al.,

55   2019; Smith et al., 2020; Boxall et al., 2022; Wallis et al., 2023). The retreat has been linked

56   primarily to increased ocean-induced bottom melting (Hogg and Gudmundsson, 2017;

57   Adusumilli et al., 2018, 2020). Along the western AP, as with major parts of the West Antarctic

58   Ice Sheet, a significant number of the outlet glaciers flow on retrograde bed slopes below sea

59   level, where mass loss due to increased atmospheric (Cook and Vaughan, 2010) and oceanic

60   warming (Pritchard et al., 2012) may be conditionally exacerbated by marine ice sheet instability

61   (MISI) (Weertman, 1974; Schoof, 2007; Gudmundsson et al., 2012; Schannwell et al., 2018).

62   Previous studies have also shown overall acceleration of western AP glaciers either for an earlier

63   epoch (Hogg and Gudmundsson, 2017) or for glaciers north of GVIIS (Wallis et al., 2023).

64

65   The largest ice shelf on the western AP, George VI Ice Shelf (GVIIS, Fig. 1), appears to be

66   thinning by excessive ocean-induced basal melting (Pritchard et al., 2012; Shepherd et al., 2012;

67   Adusumilli et al., 2018, 2020). GVIIS also experiences significant surface melt ponding in the

68   summer, primarily on the northern sector (red box in Fig. 1; Banwell et al., 2021). Previous

69   studies have identified increases in ice velocity of the glaciers and ice streams flowing into the

70   ice shelf (Hogg and Gudmundsson, 2017; Boxall et al., 2022). Rignot et al. (2019) calculated an

71   ice discharge of ~79 Gt a^{-1} between 2009 and 2017 over an area of ~ 80 M km^2 of GVIIS. This

72   was an increase from their reported discharge of ~ 78.5 Gt a^{-1} between 1999 and 2010. Modeling

73   studies suggest that the complete loss of GVIIS would trigger MISI, with a total contribution of

74   ~ 8 mm global sea level rise (Schannwell et al., 2018). Increased freshwater influx from basal

75   melting and changing coastal geometry from a thinned ice shelf will also alter ocean circulation

76   pathways in this biologically active region, and affect the Antarctic Coastal Current (Moffat et

77   al., 2008) that delivers freshwater southward to the Amundsen Sea to modify ice shelf melting

78   there (Flexas et al., 2022).

79

80   The southern and northern sections of GVIIS, which we denote as GVIIS-S and GVIIS-N

81   respectively, have distinct structure, topographic settings and connectivity to the Bellingshausen

82   Sea (see Fig. 1, and Schannwell et al. (2018), their Fig. 1), and exhibit distinct behaviors over the

83   period of satellite observations. Notably, much of GVIIS-N is fed by Palmer Land glaciers sitting

84   on a bed above sea level, whereas GVIIS-S is fed by comparatively larger glaciers from a marine

85   base (bed below sea level). The different pathways of warm Circumpolar Deep Water (CDW)

86   along troughs leading to the two calving fronts result in distinct properties of the water masses

87   driving basal melting under GVIIS-S and GVIIS-N (Jenkins and Jacobs, 2008). Strong gradients

88   of atmospheric conditions, coupling between the ocean and atmospheric forcing, and the region's

89   sensitivity to large-scale climate variability associated with the El Nino Southern Oscillation

90   (ENSO) and the Southern Annular Mode (SAM) add complexity to the drivers of mass losses for

91   each section of the ice shelf.

92

93   This complexity has led to uncertainty in the greatest risks to GVIIS. Holt et al. (2013) noted an

94   increased frequency of calving along the southern calving front and postulated that GVIIS,

95   although regarded as in no imminent danger of collapse, is more susceptible to breakup along its

96   southern margin. Nine years later, Holt and Glasser (2022) concluded that GVIIS should be

97   regarded as being on the brink of instability, with recently observed glaciological changes

98   focused on GVIIS-N.

99

100   Paleo records suggest that GVIIS previously disappeared when regional ocean and air

101   temperatures were similar to the present day (Bentley et al., 2005; Smith et al., 2007). Together

102   with marine geological data from the western AP shelf (e.g., Heroy and Anderson, 2007; Ó

103   Cofaigh et al., 2014), which demonstrates deglaciation occurred earlier in the north and

104   progressed southward, Smith et al. (2007) argued that the GVIIS retreated gradually from north

105   to south. Geological data from Moutonnée Lake, a large epishelf lake on Alexander Island (~70º

106   51'S, 68º 20'W), indicate that GVIIS disappeared in the Early Holocene (~9.6-7.7 ka before

107   present (B.P.), where present is 1950), with the onset of retreat occurring at ~9.6 ka B.P., and

108   was completely or partially reformed at this site by ~7.7 ka B.P. (Bentley et al., 2005; Smith et

109   al., 2007). Additional evidence ~120 km to the south of Moutonnée Lake (Two Step Cliffs, Fig.

110   1), suggest that the ice shelf was absent ~1.0 ka later at this site (~7.0-6.6 ka BP; Sugden and

111   Clapperton, 1981). However, limited paleo proxies exist south of GVIIS.

112

113   Several possible mechanisms leading to GVIIS collapse exist, including the well-known ones of

114   hydrofracture, and increased rifting as the ice shelf thins and shear margins weaken. Here,

115   however, we explore a new hypothesis: "Acceleration of grounded glaciers flowing into GVIIS

116   from Palmer Land is weakening GVIIS-S by increased strain-induced dynamic thinning". This

117   hypothesis reflects the possibility that grounded glaciers might accelerate due to processes

118   occurring upstream of the grounding line rather than loss of buttressing by mass reduction of the

119   ice shelf. Upstream processes include enhanced lubrication from surface melt water penetration

120   to the bed, and seawater incursions along existing subglacial channels (e.g., Chen et al., 2023).

121   We use a numerical model to show that the ice shelf will respond by generation of regions of

122   enhanced dynamic thinning, and hypothesize that this will create a positive feedback as reduced

123   buttressing from the ice shelf allows the grounded glaciers to accelerate further.

124

125   2. Study area and datasets used

126   2.1 George VI Ice Shelf (GVIIS): Setting

127   GVIIS (Fig. 1) is the largest ice shelf on the western AP (~ 23,000 km^2; Adusumilli et al., 2020).

128   GVIIS has two calving fronts ~ 450 km apart. The outlet glaciers feeding GVIIS have

129   accelerated in recent decades but grounding line positions have remained relatively stable since

130   the mid-1990s (Boxall et al., 2022). Average melt rates during 1994-2018 are ~ 4.3 ± 2.2 m a^{-1},

131   equivalent to a total meltwater flux of 88.8 ± 45.7 Gt a^{-1} (Adusumilli et al., 2020). Measurements

132   suggest a net thinning (Fricker and Padman, 2012; Paolo et al., 2015) and mass loss (Rignot et

133   al., 2013; Adusumilli et al., 2020); however, averaged over the entire ice shelf, the mass change

134   is within the range of uncertainty. The relatively high basal melt rates are driven by intrusions of

135   warm (~ 1 °C) CDW. Access holes through the ice shelf indicate that the water column is

136   strongly stratified, with a maximum temperature of ~ 1.29 °C (Middleton et al., 2022). Each

137   summer, GVIIS-N experiences extensive surface melt and persistent melt ponding (Fig. 1;

138   Banwell et al., 2021). On the Palmer Land side, the major outlet glaciers draining into GVIIS-S

139   sit on retrograde bed slopes below sea level (Fig. 1) with implications for unrestricted flow of the

140   grounded ice (through MISI) if the ice shelf disintegrates.
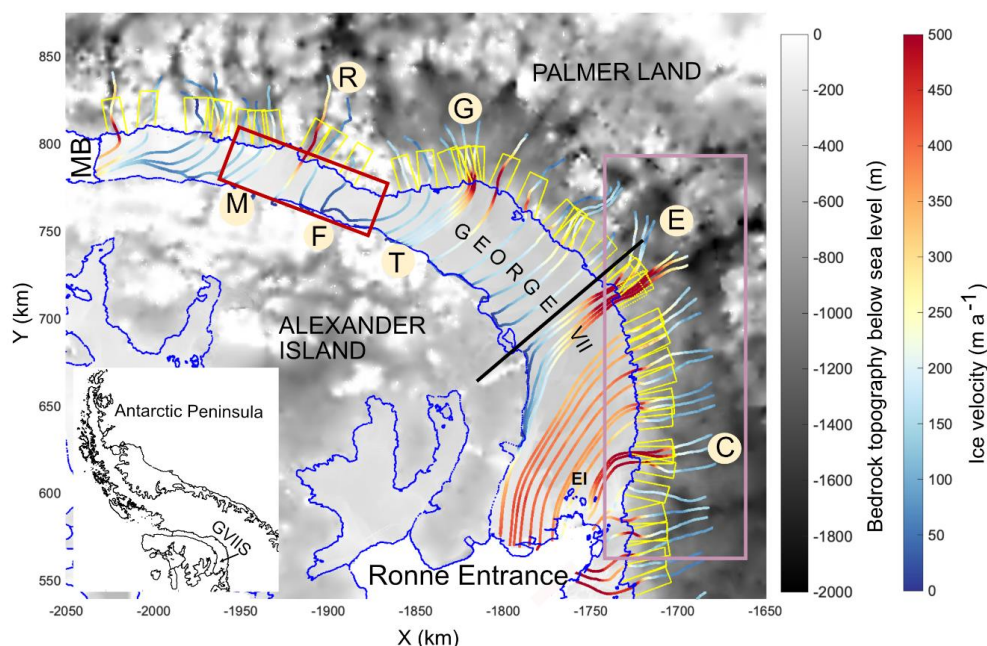
141

142   *Figure 1: George VI Ice Shelf in the AP with bed topography from BedMachine (Morlighem et*

143   *al., 2020) to identify regions below sea level, and ice velocity streamlines (2018) using ITS_LIVE*

144   *(Gardner et al., 2018). The black boxes (20×10) km extent are used for ice flux estimates.*

145   *Glaciers and locations discussed in the text are Ryder (R) and Goodenough (G) glaciers, ERS 1*

146   *and 2 (E) and Cryosat (C) ice streams, Moutonée Lake (M), Fossil Bluff (F), Two Step Cliffs (T),*

147   *Marguerite Bay (MB), and Eklund Islands (EI). Black line near E roughly follows an ice divide*

148   *and delineates the northern and southern sectors of GVIIS. The red box is the general location of*

149   *summer surface melt ponds. The purple box locates the region in the southern sector that is*

150   *identified as vulnerable in the future by modeling studies (Schannwell et al., 2018).*

151

2.2 Datasets

153 We use ice velocity data from ITS_LIVE (Gardner et al., 2018), grounding lines from SCAR and

154 InSAR compilations (Rignot et al., 2022), and ice thickness and bedrock topography from

155 BedMachine V3 (Morlighem et al., 2020). We also use ice sheet model Úa (Gudmundsson et al.,

156 2020) for strain rate calculations and experiments with basal friction (see Section 3.5). The

157 velocity fields are used to calculate the ice flow streamlines, strain rates, and dynamic thickness

158 change. Ice thickness and velocity are both used to calculate ice discharge.

159

3. Methods

161 With changing ice velocities, the dynamic components that are most likely to affect the stability

162 of an ice shelf include ice discharge rates from the grounding line ("ice flux"), effective strain

163 rates, and strain-induced dynamic thinning (also referred as "dynamic thinning"). Below we

164 describe the methodology to quantify each of these.

165

3.1 Velocity changes

167 We calculate the differences in velocity from 2013 to 2018 using $\Delta v = v(2018) -$

168 $v(2013)$ from ITS_LIVE velocities (Gardner et al., 2018) for each year. Here v(2013) and

169 v(2018) are ITS_LIVE velocities from the two years. We chose these years because complete

170 coverage of GVIIS is available only since 2013, and ITS_LIVE annual values are available only

171 up to 2018. We exclude data where the velocities are <1 m a^{-1} or > 2000 m a^{-1}, and where the

172 velocity error is >15 m a^{-1}. While these numbers are arbitrary choices, we used them because we

173 are not interested in velocities that are too slow or too fast or have a larger error associated with

174   them. Values that are too fast or too slow could also be because of artifacts in the dataset. We

175   smooth the velocity fields with a gaussian filter at 4000 m for all analyses in this work.

176

177   **3.2 Velocity streamlines**

178   We created a set of velocity streamlines (Fig. 1) that originate ~ 40 km upstream of the

179   grounding line and run along the centerline of the glaciers originating from Palmer Land using

180   built-in MATLAB functions on the 2018 ITS_LIVE velocity field. Some of the larger outlet

181   glaciers, such as the Goodenough Glacier and the ERS 1 and 2 Ice Stream, are represented by

182   more than one streamline to account for multiple tributaries and larger glacier widths (Fig. 1).

183   Since the glaciers streaming from Alexander Island onto GVIIS are much smaller, we do not

184   identify their streamlines or calculate the impact of their changing flows on the ice shelf.

185

186   **3.3 Ice shelf effective strain rates and dynamic thinning**

187   For studying the dynamic changes near the grounding zone and an ice shelf, commonly the

188   steady-state mass balance equation is invoked as in Eq. (1):

189     $\frac{\partial H}{\partial t} = -\nabla.(HU) + \dot{a} - \dot{M}_b - \dot{M}_S$ (1)

190   where H is the change in ice thickness through time t, U is the depth averaged ice velocity,

191   assumed to be the same as the observed surface velocity, $\dot{M}_S$ is the surface melt and $\dot{M}_b$ is the

192   basal melt. The first term on the right represents the strain-induced dynamic thinning term and

193   can be expanded as

194     $D = H\left(\frac{\partial u}{\partial x} + \frac{\partial v}{\partial y}\right) + \left(u\frac{\partial H}{\partial x} + v\frac{\partial H}{\partial y}\right)$ (2)

195   where u and v are the x and y components of U.

196 We assume that over an ice shelf, the vertical shear stress can be ignored (LeDoux et al., 2017);

197 therefore, the strain rates can be approximated by the terms within the first parenthesis of Eq. (2),

198 as in Das et al. (2020). The effective strain rates are second invariants of the strain rate tensor.

199 We ignore the shear components of strain rate because we are interested in the strain-induced

200 dynamic thinning, which we approximate by changes in the *x* and *y* components of ice velocity.

201 Strain-induced dynamic thinning is calculated using all the terms of Eq. (2) for each of 2013 and

202 2018. We then use the difference to estimate the rate of dynamic thickness change of the ice

203 shelf for that period.

204

3.4 Ice flux along the grounding line

206 The streamlines are roughly oriented along the fastest and thickest central parts of each glacier,

207 where the ice acceleration is also generally more pronounced. We estimate the ice fluxes, $F(t)$,

208 within the 20×10 km area around each streamline along the grounding line (Fig. 1, black boxes)

209 for each of 2013 and 2018 as the product of the mean ice velocity v_{mean} and ice thickness H_{mean}

210 and density of ice ρ=916.7 kg m^{-3}, converted to the units of Gt km^{-1} a^{-1}.

211 $$F = v_{mean} \times H_{mean} \times \rho \tag{3}$$

212 Ice flux change (ΔF) along the streamlines is then calculated as $\Delta F=F(2018)-F(2013)$. For the

213 larger glaciers, where we have multiple streamlines along the glacier, the value of ΔF around

214 each streamline is provided separately.

215

3.5. Model details

217 For model-based calculations we use the finite element ice sheet model Úa (Gudmundsson,

218 2020). This uses the Shallow-Shelf Approximation (MacAyeal, 1989), a 2-dimensional

219 approximation which integrates over depth. Ice flow is controlled by Glen's flow law (Glen,

220 1958);

221 $$\dot{\varepsilon}_{ij} = A\tau_e^{n-1}\tau_{ij} \tag{4}$$

222 where $\dot{\varepsilon}_{ij}$ are components of the strain rate tensor, A is a rate factor, τ_e is the effective stress, τ_{ij}

223 are components of the deviatoric stress tensor, and the exponent n is set equal to 3.

224

225 For basal drag, we use Weertman's sliding law (Weertman, 1957),

226 $$\tau_b = C^{-\frac{1}{m}}(\|v_b\|^2)^{\frac{1-m}{2m}} v_b \tag{5}$$
227

228 where τ_b is basal stress, C is a sliding parameter, v_b is basal velocity and the exponent m is set to

229 3.

230

231 The unstructured triangular meshes for Úa are generated using Mesh2D (Engwirda, 2014). In

232 this work we use two meshes covering the George VI area, on a rectangle with boundaries at x =

233 -2100 km and -1700 km, y = 900 km and 550 km in polar stereographic coordinates, with

234 uniform resolutions of 4 km and 10 km.

235

236 The 4-km smoothed velocities are interpolated onto each mesh, and used as the observational

237 input for an inversion process in Úa, in order to produce fields of values for basal sliding

238 parameter C and rate factor A. This method involves minimizing a cost function J of form

239 $$J = I + R, \tag{6}$$

240 where I is a misfit function given by

241 $$I = \frac{1}{2A}\int \left((u - u_{obs})/u_{err}\right)^2 dA + \frac{1}{2A}\int \left((v - v_{obs})/v_{err}\right)^2 dA \tag{7}$$

242   and R is a regularization term given by

243
$$R = \sum_{k=1,2} \frac{1}{2A} \int \left(\gamma_s^2 \left(\nabla(p_k - p_{k,prior}) \right)^2 + \gamma_a^2 (p_k - p_{k,prior})^2 \right) dA \qquad (8)$$

244

245   in which $A = \int dA$ is the total area, u and v are the modeled velocity components, u_{obs} and v_{obs}

246   are the observed velocity components, u_{err} and v_{err} are the observational errors, γ_s and γ_a are

247   slope and amplitude regularization parameters, $p_1 = log_{10} A$, $p_2 = log_{10} C$ and $p_{k,prior}$ are prior

248   values, or initial estimates, for the parameters p_k. More details on the inversion process in Úa

249   can be found in Barnes et al. (2021) and its applications in Das et al. (2023).

250

251   The inversion outputs are used in calculations of velocities within the model. These are snapshot

252   calculations with no time dependence, using the geometry from BedMachine and not evolving

253   the ice thickness. The velocities are calculated in three different cases. Firstly, we use the

254   original inversion outputs, fields of values for A and C derived from the process described above.

255   To investigate the effect of variability in basal friction, which is an uncertainty within the model

256   as it is not an observed quantity, we perform two more calculations with the values of C across

257   the entire domain multiplied by 0.95 (a 5% reduction in the sliding parameter) and by 1.05 (a 5%

258   increase to the sliding parameter). For all the calculated velocities, the components of the strain

259   rate tensor are then calculated as stated in section 3.3. Within the model domain, the calculation

260   is performed on six integration points within each finite element, defined by Gauss-Jacobi

261   quadrature.

262   **3.6 Strain rate and qualitative length-scale analysis**

263   The appropriate length-scales for smoothing the velocity fields and calculating strain rates is an

264   ongoing topic of much discussion (e.g. Alley et al., 2018). On Ross Ice Shelf, Das et al. (2020)

265   used a 15 km velocity smoothing window to calculate strain rates, based on scales of

266   uncertainties in both ice thickness and velocity. However, it is not necessarily easy to identify

267   what grid resolution is needed for ice shelves. Because of the size of GVIIS and its smaller ice

268   streams and glaciers, a 15 km grid will undesirably smooth out the dynamic changes of the

269   individual glaciers. To assess length-scales (e.g., Alley et al., 2018), we calculate strain rates

270   using a 4 km square grid using ITS_LIVE velocities explained in the previous sections and

271   compare with a 4 and 10 km grid calculated using the ice flow model Úa, also described in the

272   previous sections.

4. Results

4.1 Velocity changes on the GVIIS grounding zone and on the ice shelf

275   The change in velocity from 2013 to 2018 within the 20×10 km boxes defining grounded glacier

276   and ice stream outlets (Fig. 2) show a coherent increase in annual velocity during this period on

277   many of the outlet glaciers from Palmer Land side of GVIIS. The average velocity increase (Δv)

278   between 2013 and 2018 is ~ 16 m a^{-1} (~ 8%) within all the boxes. We express the velocity

279   increase (Δv) as a percentage change from 2013 in Fig. 2a to demonstrate the significance. The

280   actual Δv along the streamlines of the major outlet glaciers are shown in the panels of Fig. 2b-c.

281   These outlet glaciers are among the fastest changing regions of GVIIS. The average Δv on the

282   ice shelf is ~ 12 m a^{-1} (~ 7%) with the southern sector experiencing a larger Δv than the northern

283   sector. The area within these boxes covers the grounding zone as well as an extended section

284   upstream along the centerline of each glacier. The velocity increase over the ERS Ice Stream

285   grounding zone is one of the larger increases on GVIIS with an average of ~ 33.4 m a^{-1} (Fig. 2a,

286   c). The mean velocity increase of the glaciers located immediately south of ERS and north

287   CryoSat (between E1 and C1 streamlines, Fig. 2a-b) is ~ 44 m a^{-1}. This region between ERS and

288   Cryosat ice streams is experiencing the largest velocity increase on the ice shelf. This region on

289   the ice shelf is almost freely floating without impinging on either Alexander or Eklund Islands

290   and is important for the stability of GVIIS-S.

291
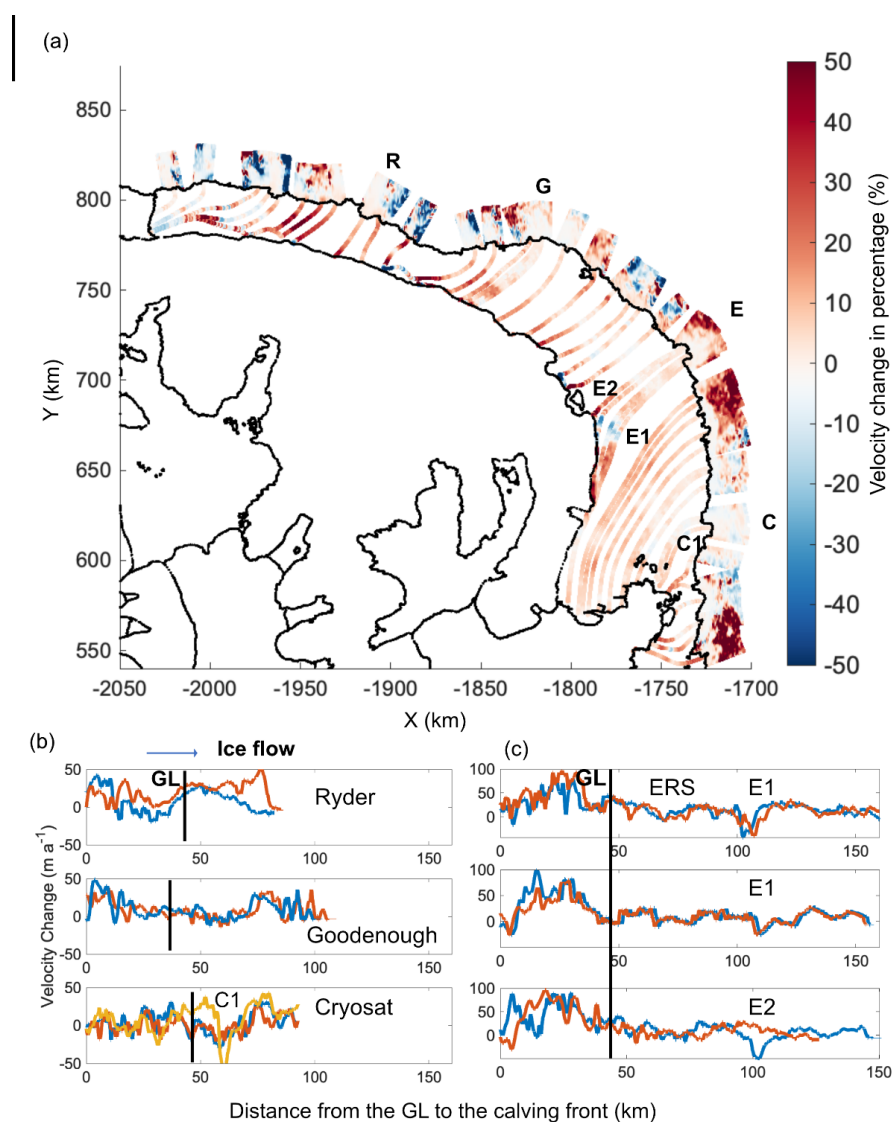
Figure 2: ITS_LIVE velocity on grounding zone of GVIIS glaciers: (a) Difference in velocity (%)

between 2013 and 2018 along the 20×10 km boxes in Fig. 1 along the grounding zones and

294   *streamlines on the ice shelf. The major glaciers include the Ryder Glacier (R), the Goodenough*

295   *Glacier (G), the ERS 1 and 2 ice stream (E) and the CryoSat Ice Stream (C); (b) Velocity*

296   *difference (Δv) between 2013 and 2018 for Ryder, Goodenough glaciers and CryoSat Ice*

297   *Stream; (c) Δv between 2013 and 2018 on the ERS 1 and 2 ice streams. The black line shows the*

298   *approximate position of the GL from Fig. 1.*

299

300   The mean velocity increase along the grounding zones of the other larger glaciers including

301   Goodenough (G) Ryder (R), and CryoSat (C) is ~ 8 m a^{-1} (Fig. 2a, b). Unlike other ice shelves,

302   the velocity does not keep increasing in the direction of ice flow along the streamlines as ice

303   moves away from the grounding zone (Fig. 2a, 2b-c). GVIIS is unique because ice sourced from

304   some glaciers from the Palmer Land side impinge on Alexander and Eklund Islands, and the non-

305   uniform velocity response likely results from the backstress these glaciers receive from the

306   grounded regions. In the case of the ERS Ice Stream and the glaciers south of it, the velocity

307   increase upstream is > 30% (Fig. 2a). While the source of velocity increase for ERS and glaciers

308   south of it is unknown, we speculate that the surface meltwater reaching the bed near Ryder

309   Glacier (Pedley et al., 1988) provides the basal lubrication required for local acceleration at the

310   grounding zone, which slows further downstream (Fig. 2b).

311

312   **4.2 Effective strain rates of GVIIS during 2013 and 2018**

313   Estimates of strain rates (units of a^{-1}) from ITS_LIVE velocities (4 km, Fig. 3 a-b) and strain

314   rates from modeled velocities in Úa (4 km, Fig. 3c–3d; 10 km Fig. 3e–3f) show similar large-

315   scale spatial patterns and variabilities in the observed and modeled values. The observed sets are

316   more detailed, although has a higher likelihood of noise. The strain rate fields calculated from Úa

317   are smoother, as noise in the observations is removed by regularization within the inversion

318   process. This means that the strain fields from Úa show less detail than the observations, but are

319   useful for capturing large scale patterns more clearly. Here, positive sign indicates divergence

320   implying strain thinning and negative sign indicates compressive strain rates that lead to

321   localized thickening of the ice shelf. On GVIIS-S, dynamic thinning is experienced in the region

322   bordered by ERS (E) and CryoSat (C) ice streams (Fig. 3). The velocity increase of this band is

323   discussed in Section 4.1.

324

325
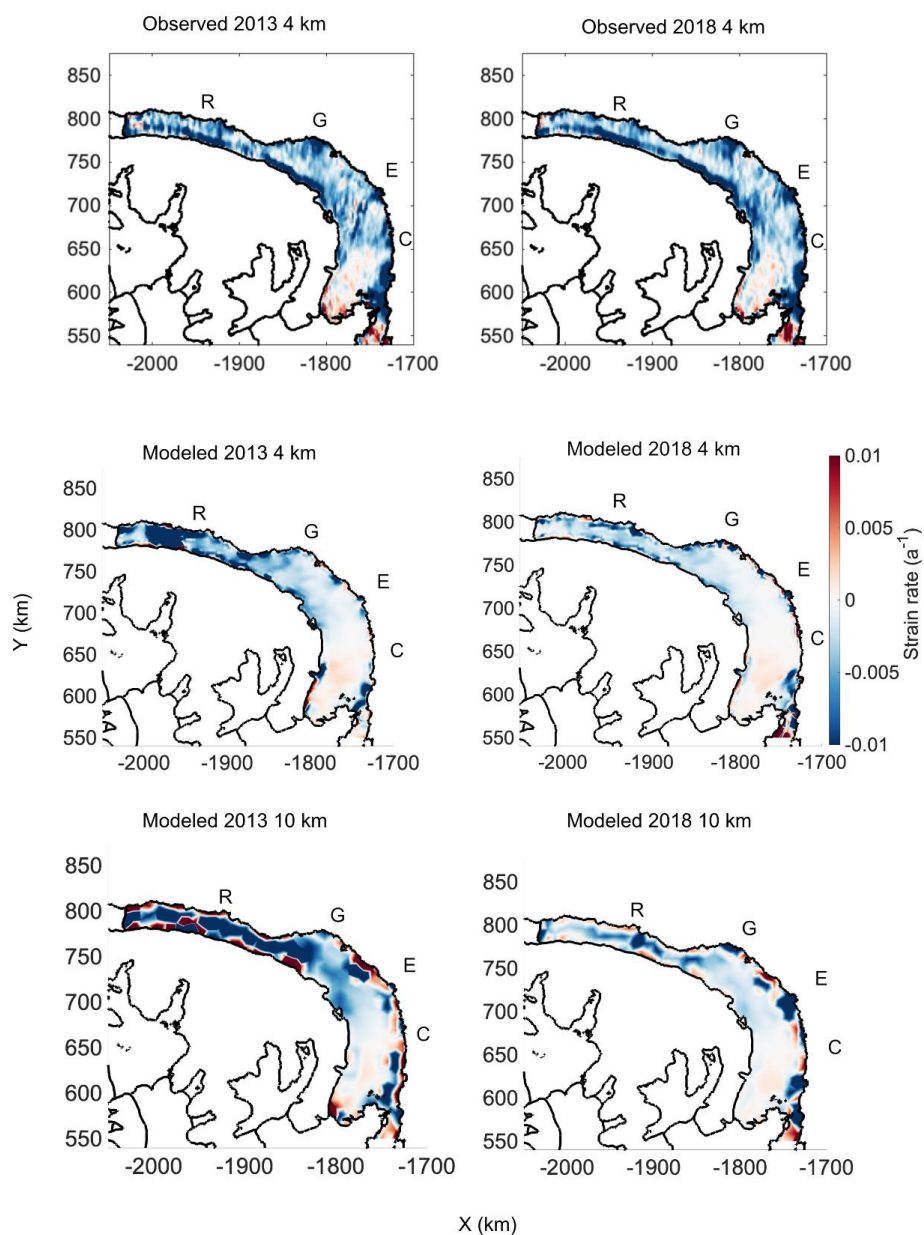
Figure 3: Strain rates calculated at 4 km and 10 km grid spacing (a) for 2013 using ITS_LIVE

326

(b) for 2018 using ITS_LIVE (c) Strain rates simulated using Úa for 2013 at 4 km (d) Strain

327

328   *rates simulated using Úa for 2018 at 4 km (e) Strain rates simulated using Úa for 2013 at 10 km*

329   *(f) Strain rates simulated using Úa for 2018 at 10 km.*

330

331   **4.3 Length scales of effective strain rates on GVIIS**

332   For this work, we use a 4-km length scale for all analyses, as a compromise between

333   measurement noise and width of individual glaciers and ice streams (see Section 3.6). We also

334   calculate strain rates on a 10 km mesh using Úa (Fig. 3e-f). The 10 km strain rate product is

335   smoother than the 4 km product, but we lose information of the small-scale variations in strain

336   rates. In this work, we use the 4 km grid for both observation-based and modeled strain rates to

337   calculate dynamic thinning to preserve the local variability of strain rates that are difficult to

338   observe in the 10 km grid.

339

340   **4.4 Increased ice flux across Palmer Land grounding zone and dynamic thickness change**

341   Most outlet glaciers have experienced increased ice flux between 2013 and 2018 along the 20×10

342   km boxes near the grounding line for each streamline, particularly on the GVIIS-S sector that

343   also has thicker ice (Fig. 4a) and a submarine, retrograde bed (Fig. 1). ERS Ice Stream is the

344   largest ice stream on the ice shelf, and is experiencing one of the highest increases in ice flux ΔF

345   by 21 ± 19 Gt km^{-1} a^{-1} between 2013 and 2018 (Fig. 4a). The glaciers bounded by ERS and

346   Cryosat forming the freely floating region discussed earlier has an average ΔF of 20 ± 11 Gt km^{-1}

347   a^{-1}, also a high value similar to ERS Ice Stream. Cryosat, Ryder and Goodenough each

348   experienced flux increases during the same period, with ΔF values of 2.4 ± 2.4, 2.4 ± 2.2, 5 ± 4.3

349   Gt km^{-1} a^{-1}, respectively. The mean ΔF during 2013–2018 for all the 20×10 km boxes of GVIIS

350   were 8.9 ± 6.8 Gt km^{-1} a^{-1}. Our results show that the strain-induced dynamic thickness change

351 increases progressively from north to south (Fig. 4b). Near the Eklund Islands, where recent

352 calving events have concentrated, the strain-induced dynamic thickness change between 2013

353 and 2018 is ~ 2 m a^{-1}, (Fig. 4b) and is of the same order of magnitude as the basal melting rates

354 from previous studies.

355

356
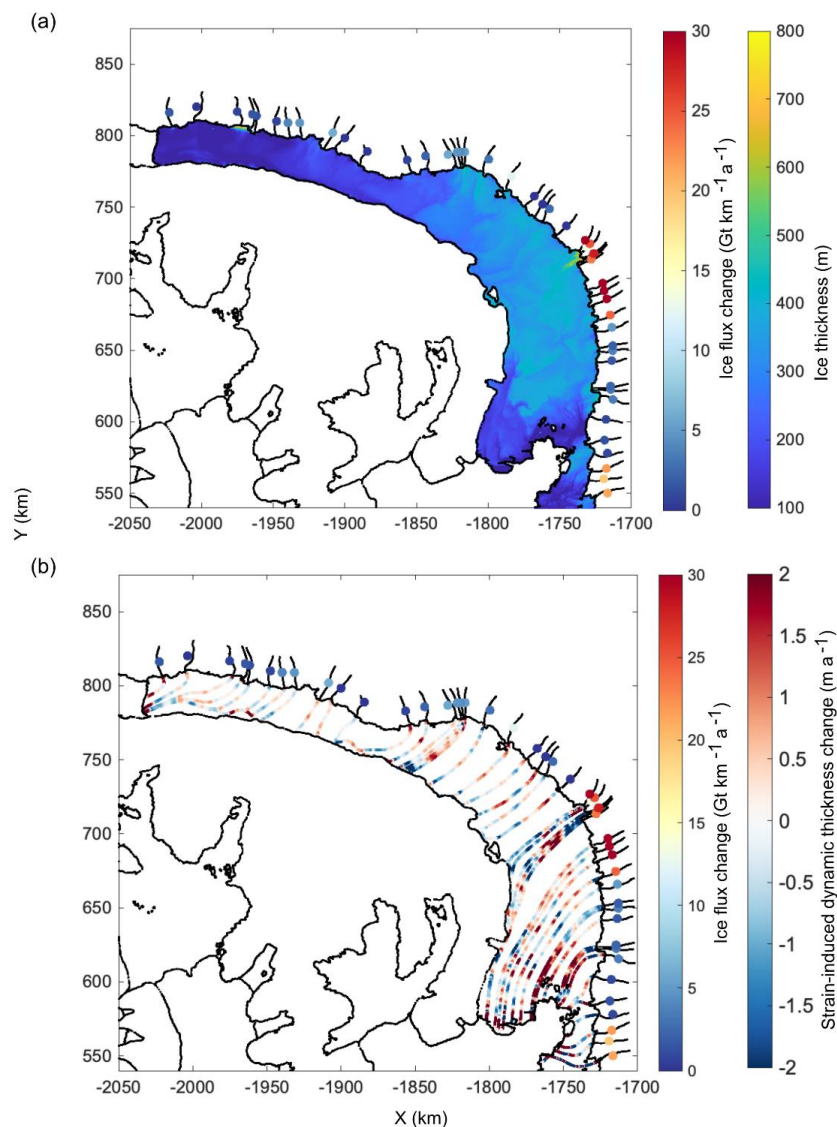
Figure 4: Ice flux change (ΔF) along the grounding zone of the glaciers and strain-induced

dynamic thickness change on GVIIS. (a) Circles upstream of the grounding zone indicate

changes in ice flux (ΔF) between 2013 and 2018 along the 20×10 km boxes around the

streamlines of the outlet glaciers in Gt km^{-1} a^{-1}. Filled color on the ice shelf: ice thickness (m).

361   *(b) Circles on grounded streamlines: as in panel (a). Colored streamlines: Observation-based*

362   *strain-induced dynamic thickness change rates (using 4 km strain rate values from Fig. 3a-b) on*

363   *the ice shelf (m a⁻¹).*

364

4.5. Changes in modeled strain rates of GVIIS with changes in basal friction C

366   We carry out some simple simulations to investigate the effect of changing basal sliding, which

367   can be seen as a proxy for basal lubrication due to subglacial discharge resulting in a scenario

368   where ice velocity at the grounding zone increase. Taking the output from an inversion in Úa, we

369   change the basal sliding parameter by 5% in each direction and recalculate strain rates from the

370   resulting modeled velocity fields. The results are shown in Fig. 5a–b. When the sliding

371   parameter is increased, the increase in velocity of the glaciers flowing into GVIIS results in a

372   more compressive regime in the narrow northern section (Fig. 5b), comparatively little overall

373   change in the strain on the southern sector, and a more divergent regime in the Ronne Entrance.

374   Part of the southern sector does have a slight divergence signal, although much lower in

375   magnitude than the changes elsewhere in the domain, on the order of 10^{-5} a^{-1}. When lowering the

376   basal sliding, the opposite is true, although it is not clear what actual processes could result in a

377   higher value of *C*. The modeled velocities used in this case are calculated instantaneously with a

378   new value of *C* on the same geometry, but if allowed to evolve over time differences in thickness

379   may also result, which could lead to further changes in the strain regimes.

380
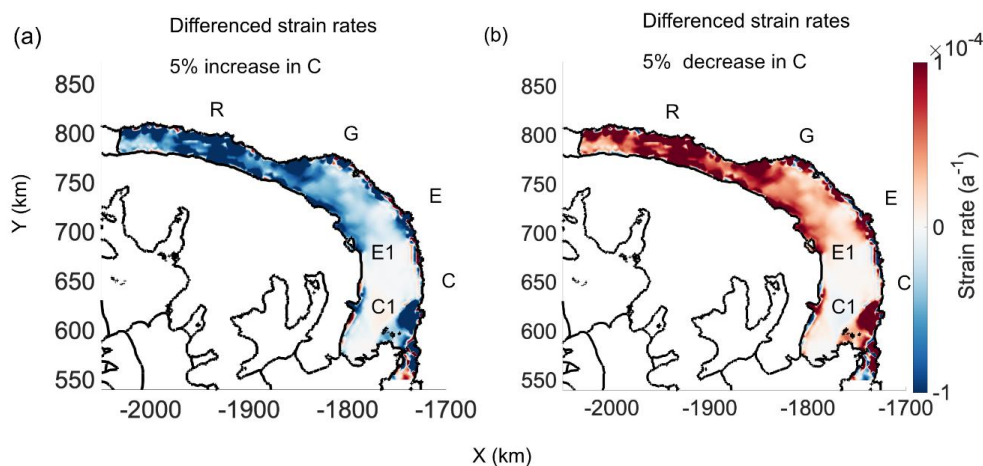
Figure 5: Strain rate (a⁻¹) differences Original- percent changes in the value of C using Úa (a)

5% increase and (b) 5% decrease in C from the original shows only the northern half (north of

streamline E1) is sensitive to changes ice flux across the grounding line in the shorter term.

5. Discussion

The observed increase in velocity at the grounding zone and on the ice shelf from 2013 to 2018

is consistent with Boxall et al. (2022), who used Copernicus Sentinel 1A/B between 2014 and

2020 over GVIIS outlet glaciers. Their austral summer velocity increase rates of ~ 22 m a⁻¹ and ~

15% increase near the grounding zone is consistent with our mean annual velocity change of ~

16 m a⁻¹ during 2013-2018 along the grounding zones of the Palmer Land outlet glaciers.

Furthermore, between 1992 and 2015, a 13% increase in ice velocity was observed on the

Western Palmer Land (Hogg et al., 2017).

The error estimates are calculated separately for the strain thinning and ice flux as follows:

$$\epsilon_{Flux} = \Delta F_{mean} \sqrt{\left[\left(\frac{\epsilon_{velocity2013}}{M_{velocity2013}}\right)^2 + \left(\frac{\epsilon_{velocity2018}}{M_{velocity2018}}\right)^2 + \left(\frac{\epsilon_{IceThickness}}{M_{IceThickness}}\right)^2\right]} \tag{9}$$

where ϵ_{Flux} is the error in ice flux in Gt km^{-1} a^{-1}, ΔF_{mean} is the mean flux change within the
20×10 km boxes, ϵ is the standard deviations of the various components, M is the mean of the
various components used in calculating the ice flux.
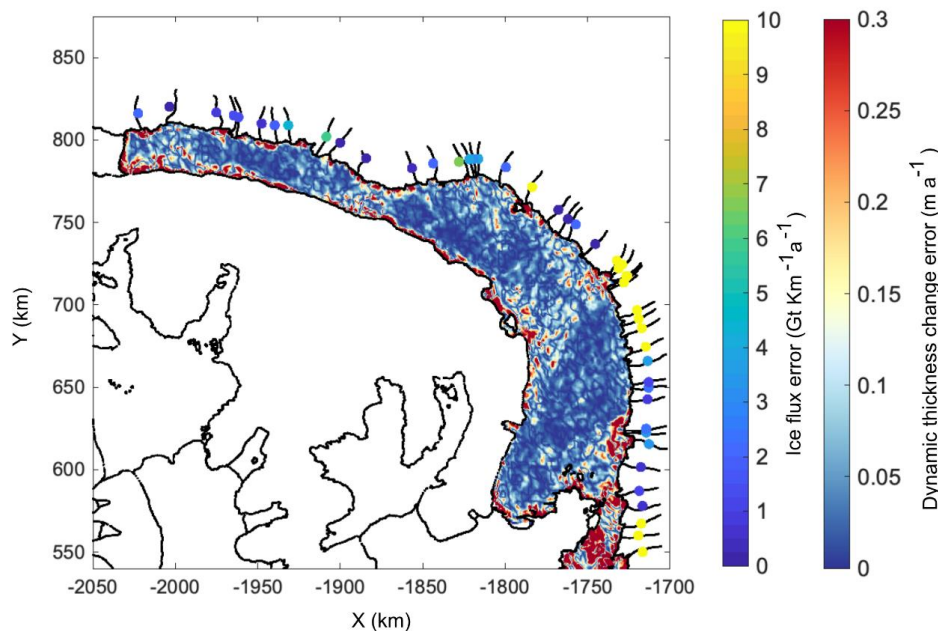
Figure 6: Error estimates in dynamic thickness change on the ice shelf and ice flux calculated

within each 20×10 boxes

The errors in dynamic thinning are calculated for each component of velocity for both 2013 and
2018. The error in ice thickness is counted twice because of the two years used in dynamic
thinning calculations.

410 $\epsilon_{DT} =$

411 $$\sqrt{D_{diff}^2 \left[\left(\frac{\epsilon_{Xvelocity2013}}{M_{Xvelocity2013}} \right)^2 + \left(\frac{\epsilon_{Yvelocity2013}}{M_{Yvelocity2013}} \right)^2 + 2 \left(\frac{\epsilon_{IceThickness}}{M_{IceThickness}} \right)^2 + \left(\frac{\epsilon_{Xvelocity2018}}{M_{Xvelocity2018}} \right)^2 + \left(\frac{\epsilon_{Yvelocity2018}}{M_{Yvelocity2018}} \right)^2 \right]}$$

412 (10)

413 where ϵ_{DT} is the error in dynamic thinning (m a^{-1}), D_{diff} is the difference in dynamic thinning

414 between 2013 and 2018, ϵ terms within the square root are the standard deviations of the various

415 components, and the M components are the average values of those components.

416

417 Our error ranges for ice fluxes are quite high for some regions because of the large variability of

418 the velocity and ice thickness along the 20×10 km boxes (Fig. 6). These boxes are located

419 roughly along the centerlines of the glaciers where the variability in both ice thickness and

420 velocity are the highest. The standard deviation of velocity within the 20×10 regions is the

421 largest contributor of errors in our estimates. The dynamic thinning, on the other hand, is

422 calculated only on the ice shelf where the variability of ice thickness and velocity changes are

423 relatively smaller than the grounding zone areas, and therefore the errors in dynamic thinning are

424 also low.

425

426 An important simulation experiment shows that with little decrease in basal friction *C* upstream

427 of the grounding zone, GVIIS-N becomes more compressive. We anticipate that as ice flux

428 increases in the northern sector, the ice shelf may temporarily become more compressive until

429 ice loss also increases through the calving front. GVIIS-N has less occurrences of fractures

430 despite the presence of pervasive melt ponds, primarily due to its compressive stress regime.

431 This might suggest that although the ice flux and the prevalence of melt ponds increases, the

432 northern part may be resistant to hydrofracture, at least until competing processes take over.

433   On the other hand, the same basal friction *C* simulation shows that GVIIS-S continues to

434   experience diverging ice strain rates independent of the changes in basal friction. The southern

435   calving edge is also identified by Fürst et al., (2016) as a vulnerable part of the ice shelf. This

436   sector also experiences extensive basal melting on the order of ~ 3-4 m a^{-1} (Adusumilli et al.,

437   2020; 2018) due to warmer ocean temperatures at depth (Giulivi et al., 1997; Jenkins and Jacobs,

438   2008). Our estimates of strain-induced dynamic thickness change rates of ~ 2 m a^{-1} or higher is

439   comparable to the basal melt rates here. The southern sector has thicker ice and has larger ice

440   streams located on retrograde bed slopes below sea level (Fig. 1). Based on these results, we

441   suggest that in the near future, GVIIS-S is more susceptible to unstable changes, and ice

442   dynamics precondition the ice shelf for a rapid retreat.

443

444   However, this contrasts with the Early Holocene retreat of GVIIS that is hypothesized to have

445   progressed from north to south (Smith et al., 2007). The period of absence of George VI Ice

446   Shelf between ~9.6-7.7 ka B.P, immediately postdates evidence for warmer sea surface

447   temperatures (Shevenell et al., 2011; Etourneau et al., 2013) and ice core evidence of a

448   widespread Early Holocene climatic optimum ~11.5-9.0 ka B.P (Masson et al., 2000; Mulvaney

449   et al., 2012). These results, interpreted through modern observations of basal melting and

450   surface melt water ponding, suggest that the Early Holocene retreat was driven by a combination

451   of surface and basal melting. Similar warming conditions exist on GVIIS in recent years as well,

452   and are believed to be the primary drivers of modern ice shelf mass loss.

453

454   Dynamic thinning redistributes mass on an ice shelf, and thinning in vulnerable regions and

455   retreats of ice fronts will make the ice shelf dynamically unstable. The relative roles of

456 hydrofracture of the northern, thinner portion of the ice shelf and the reduced buttressing of the

457 large fluxes from the relatively larger southern glaciers and ice streams will determine whether

458 future loss proceeds from the north or the south.

459

460 **6. Conclusions**

461 In this work we use satellite remote sensing data and numerical modeling to examine the

462 vulnerability of George VI Ice Shelf, Antarctic Peninsula that has been undergoing extensive

463 basal melting and has been recently deemed unstable. We observe increased strain induced

464 dynamic thickness change on the southern sector of GVIIS of > 2 m a^{-1} which is comparable to

465 the basal melt rates from previous satellite-derived estimates and demonstrate the importance of

466 dynamic changes on an ice shelf. Our observations of strain-induced dynamic thickness change,

467 ice velocity and ice flux increase across the grounding zone of the southern part of George VI

468 shows that it is currently more vulnerable than the northern sector. This is in sharp contrast to

469 limited paleo observations that suggest that the early Holocene retreat of George VI proceeded

470 from North to South, and both atmospheric and ocean conditions were responsible for the

471 disintegration. To explore the dynamic differences between GVIIS-N and GVIIS-S, we use a

472 numerical model and change the basal friction parameter C by 5% in either directions. We find

473 that even with this small reduction in C, the northern sector becomes more compressive, which

474 makes it resistant to hydrofracture despite the proliferation of surface melt ponds there. On the

475 other hand, the southern sector continues to experience diverging strain rates for the same

476 numerical setup. Based on our observations of change in velocity, ice flux and dynamic thinning,

477 we conclude that: basal lubrication of southern glaciers and ice streams may increase grounded

478 ice loss; and a positive feedback between ice discharge and dynamic thinning on vulnerable

479   regions of an ice shelf can act over short time scales to precondition the ice shelf collapse in the

480   future.

481

Data Availability

483   ITS_LIVE velocity data used in this analysis is available at https://its-live.jpl.nasa.gov, and

484   BedMachine V3 data at https://nsidc.org/data/nsidc-0756/versions/3. All datasets used in this

485   work will be deposited at the project page in USAP-DC repository. For review, we have

486   temporarily uploaded the datasets and codes in Mendeley for review purposes only

487   https://data.mendeley.com/preview/2vdv9hvgwv?a=6456bae5-a794-42da-966b-5718c7453c67.

488   Please note these files are not final, and will change according to reviewers' comments. DOI

489   reserved but not active: doi: 10.17632/2vdv9hvgwv.1

490

491   **Author Contributions:** ID developed the concept, methodology, worked on the observations,

492   interpreted the results and wrote the manuscript; JB carried out the modeling aspects of this work

493   and contributed to writing of the manuscript, JS and SH interpreted the paleo aspects of GVIIS,

494   and contributed to writing of the manuscript, RC provided data processing support and

495   contributed towards writing the manuscript, LP co-developed the methodology and

496   interpretations with ID, and contributed to writing the manuscript. All authors commented on the

497   manuscript.

498

499   **Competing interests:**

500   The authors declare that they have no conflict of interests.

501

Acknowledgements

502

503 This work was funded by NASA Cryosphere 80NSSC21K0747 to ID and LP, and NSF grant

504 OPP 20-35078 to ID. The authors thank Keith Nicholls, Susan Howard and Ece Bilen for help

505 during preparation of the manuscript.

506

507

508

References

510 Adusumilli, S., Fricker, H. A., Siegfried, M. R., Padman, L., Paolo, F. S., and Ligtenberg, S. R.

511   M.: Variable Basal Melt Rates of Antarctic Peninsula Ice Shelves, 1994–2016, Geophys

512   Res Lett, 45, 4086–4095, https://doi.org/10.1002/2017gl076652, 2018.

513 Adusumilli, S., Fricker, H. A., Medley, B., Padman, L., and Siegfried, M. R.: Interannual

514   variations in meltwater input to the Southern Ocean from Antarctic ice shelves, Nat Geosci,

515   13, 616–620, https://doi.org/10.1038/s41561-020-0616-z, 2020.

516 Alley, K. E., Scambos, T. A., Miller, J. Z., Long, D. G., and MacFerrin, M.: Quantifying

517   vulnerability of Antarctic ice shelves to hydrofracture using microwave scattering

518   properties, Remote Sens Environ, 210, 297–306,

519   https://doi.org/https://doi.org/10.1016/j.rse.2018.03.025, 2018.

520 Banwell, A. F., Datta, R. T., Dell, R. L., Moussavi, M., Brucker, L., Picard, G., Shuman, C. A.,

521   and Stevens, L. A.: The 32-year record-high surface melt in 2019/2020 on the northern

522   George VI Ice Shelf, Antarctic Peninsula, Cryosphere, 15, 909–925,

523   https://doi.org/10.5194/tc-15-909-2021, 2021.

524 Barnes, J. M., dos Santos, T., Goldberg, D., Gudmundsson, G. H., Morlighem, M., and De Rydt,

525   J.: The transferability of adjoint inversion products between different ice flow models,

526   Cryosphere, 15, 1975–2000, https://doi.org/10.5194/tc-15-1975-2021, 2021.

527   Bentley, M. J., Hodgson, D. A., Smith, J. A., and Cox, N. J.: Relative sea level curves for the

528   South Shetland Islands and Marguerite Bay, Antarctic Peninsula, Quat Sci Rev, 24, 1203–

529   1216, https://doi.org/https://doi.org/10.1016/j.quascirev.2004.10.004, 2005.

530   Boxall, K., Christie, F. D. W., Willis, I. C., Wuite, J., and Nagler, T.: Seasonal land-ice-flow

531   variability in the Antarctic Peninsula, Cryosphere, 16, 3907–3932,

532   https://doi.org/10.5194/tc-16-3907-2022, 2022.

533   Chen, H., Rignot, E., Scheuchl, B., and Ehrenfeucht, S.: Grounding zone of Amery Ice Shelf,

534   Antarctica, from differential synthetic-aperture radar interferometry. *Geophysical Research*

535   *Letters*, *50*, e2022GL102430. https://doi.org/10.1029/2022GL102430, 2023.

536   Cook, A. J. and Vaughan, D. G.: Overview of areal changes of the ice shelves on the Antarctic

537   Peninsula over the past 50 years, Cryosphere, 4, 77–98, https://doi.org/10.5194/tc-4-77-

538   2010, 2010.

539   Das, I., Padman, L., Bell, R. E., Fricker, H. A., Tinto, K. J., Hulbe, C. L., Siddoway, C. S.,

540   Dhakal, T., Frearson, N. P., Mosbeux, C., Cordero, S. I., and Siegfried, M. R.: Multidecadal

541   Basal Melt Rates and Structure of the Ross Ice Shelf, Antarctica, Using Airborne Ice

542   Penetrating Radar, J Geophys Res Earth Surf, 125, e2019JF005241,

543   https://doi.org/10.1029/2019JF005241, 2020.

544   Das, I., Morlighem, M., Barnes, J., Gudmundsson, G. H., Goldberg, D., and Dias dos Santos, T.:

545   In the Quest of a Parametric Relation Between Ice Sheet Model Inferred Weertman's

546   Sliding-Law Parameter and Airborne Radar-Derived Basal Reflectivity Underneath

547   Thwaites Glacier, Antarctica, Geophys Res Lett, 50, e2022GL098910,

548   https://doi.org/https://doi.org/10.1029/2022GL098910, 2023.

549   Engwirda, D.: Locally optimal Delaunay-refinement and optimisation-based mesh generation.

550   Ph.D. thesis, School of Mathematics and Statistics, The University of Sydney, 2014.

551   Etourneau, J., Collins, L. G., Willmott, V., Kim, J.-H., Barbara, L., Leventer, A., Schouten, S.,

552   Sinninghe Damsté, J. S., Bianchini, A., Klein, V., Crosta, X., and Massé, G.: Holocene

553   climate variations in the western Antarctic Peninsula: evidence for sea ice extent

554   predominantly controlled by changes in insolation and ENSO variability, Climate of the

555   Past, 9, 1431–1446, https://doi.org/10.5194/cp-9-1431-2013, 2013.

556   Flexas, M. M., Thompson, A. F., Schodlok, M. P., Zhang, H., and Speer, K.: Antarctic Peninsula

557   warming triggers enhanced basal melt rates throughout West Antarctica, Sci Adv, 8,

558   eabj9134, https://doi.org/10.1126/sciadv.abj9134, 2022.

559   Fürst, J. J., Durand, G., Gillet-Chaulet, F., Tavard, L., Rankl, M., Braun, M., and Gagliardini, O.:

560   The safety band of Antarctic ice shelves, Nat Clim Chang, 6, 479,

561   https://doi.org/10.1038/nclimate2912

562   https://www.nature.com/articles/nclimate2912#supplementary-information, 2016.

563   Fricker, H. A., and Padman, L.: Thirty years of elevation change on Antarctic Peninsula ice

564   shelves from multimission satellite radar altimetry, *Journal of Geophysical Research --*

565   *Oceans*, *117*, C02026, doi:10.1029/2011JC007126, 2012

566   Gardner, A. S., Moholdt, G., Scambos, T., Fahnstock, M., Ligtenberg, S., van den Broeke, M.,

567   and Nilsson, J.: Increased West Antarctic and unchanged East Antarctic ice discharge over

568   the last 7 years, Cryosphere, 12, 521–547, https://doi.org/10.5194/tc-12-521-2018, 2018.

569   Giulivi, C.F. and Jacobs S.S.: Oceanographic data in the Amundenden and Bellingshausen Seas:

570   N.B. Palmer cruise 9402, Febreuary-March 1994. Lamont-Doherty Earth Observatory Tech

571   Rep. 97-3, 330 pp, 1997.

572   Glen, J.: The flow law of ice: A discussion of the assumptions made in glacier theory, their

573   experimental foundations and consequences. IASH Publ., 47, 171–183, 1958

574   Gudmundsson, G. H., Krug, J., Durand, G., Favier, L., and Gagliardini, O.: The stability of

575   grounding lines on retrograde slopes, Cryosphere, 6, 1497–1505, https://doi.org/10.5194/tc-

576   6-1497-2012, 2012.

577   Gudmundsson, G. H. (2020) GHilmarG/UaSource: Ua2019b (Version

578   v2019b), https://doi.org/10.5281/zenodo.3706623

579   Heroy, D. C. and Anderson, J. B.: Radiocarbon constraints on Antarctic Peninsula Ice Sheet

580   retreat following the Last Glacial Maximum (LGM), Quat Sci Rev, 26, 3286–3297,

581   https://doi.org/https://doi.org/10.1016/j.quascirev.2007.07.012, 2007.

582   Hogg, A. E. and Gudmundsson, G. H.: Impacts of the Larsen-C Ice Shelf calving event, Nat

583   Clim Chang, 7, 540–542, https://doi.org/10.1038/nclimate3359, 2017.

584   Holt, T. and Glasser, N. F.: Changes in area, flow speed and structure of southwest Antarctic

585   Peninsula ice shelves in the 21st century, Journal of Glaciology, 1–19, https://doi.org/DOI:

586   10.1017/jog.2022.7, 2022.

587   Holt, T. O., Glasser, N. F., Quincey, D. J., and Siegfried, M. R.: Speedup and fracturing of

588   George VI Ice Shelf, Antarctic Peninsula, Cryosphere, 7, 797–816,

589   https://doi.org/10.5194/tc-7-797-2013, 2013.

590   Jenkins, A. and Jacobs, S.: Circulation and melting beneath George VI Ice Shelf, Antarctica, J

591   Geophys Res Oceans, 113, https://doi.org/10.1029/2007jc004449, 2008.

592   LeDoux, C. M., Hulbe, C. L., Forbes, M. P., Scambos, T. A., and Alley, K.: Structural provinces

593   of the Ross Ice Shelf, Antarctica, Ann Glaciol, 58, 88–98,

594   https://doi.org/10.1017/aog.2017.24, 2017.

595   Li, R., Cheng, Y., Chang, T., Gwyther, D. E., Forbes, M., An, L., Xia, M., Yuan, X., Qiao, G.,

596   Tong, X., and Ye, W.: Satellite record reveals 1960s acceleration of Totten Ice Shelf in East

597   Antarctica, Nat Commun, 14, 4061, https://doi.org/10.1038/s41467-023-39588-x, 2023.

598   MacAyeal, D. R.: Large-scale ice flow over a viscous basal sediment: Theory and application to

599   ice stream B, Antarctica, J Geophys Res Solid Earth, 94, 4071–4087,

600   https://doi.org/10.1029/JB094iB04p04071, 1989.

601   Masson, V., Vimeux, F., Jouzel, J., Morgan, V., Delmotte, M., Ciais, P., Hammer, C., Johnsen,

602   S., Lipenkov, V. Ya., Mosley-Thompson, E., Petit, J.-R., Steig, E. J., Stievenard, M., and

603   Vaikmae, R.: Holocene Climate Variability in Antarctica Based on 11 Ice-Core Isotopic

604   Records, Quat Res, 54, 348–358, https://doi.org/https://doi.org/10.1006/qres.2000.2172,

605   2000.

606   Middleton, L., Davis, P. E. D., Taylor, J. R., and Nicholls, K. W.: Double Diffusion As a Driver

607   of Turbulence in the Stratified Boundary Layer Beneath George VI Ice Shelf, Geophys Res

608   Lett, 49, e2021GL096119, https://doi.org/https://doi.org/10.1029/2021GL096119, 2022.

609   Moffat, C., Beardsley, R. C., Owens, B., & Van Lipzig, N.: A first description of the Antarctic

610   Peninsula Coastal Current. *Deep Sea Research Part II: Topical Studies in Oceanography*,

611   *55*(3-4), 277-293, 2008.

612   Morlighem, M., Rignot, E., Binder, T., Blankenship, D., Drews, R., Eagles, G., Eisen, O.,

613   Ferraccioli, F., Forsberg, R., Fretwell, P., Goel, V., Greenbaum, J. S., Gudmundsson, H.,

614   Guo, J., Helm, V., Hofstede, C., Howat, I., Humbert, A., Jokat, W., Karlsson, N. B., Lee,

615   W. S., Matsuoka, K., Millan, R., Mouginot, J., Paden, J., Pattyn, F., Roberts, J., Rosier, S.,

616   Ruppel, A., Seroussi, H., Smith, E. C., Steinhage, D., Sun, B., Broeke, M. R. van den,

617   Ommen, T. D. van, Wessem, M. van, and Young, D. A.: Deep glacial troughs and

618   stabilizing ridges unveiled beneath the margins of the Antarctic ice sheet, Nat Geosci, 13,

619   132–137, https://doi.org/10.1038/s41561-019-0510-8, 2020.

620   Mulvaney, R., Abram, N. J., Hindmarsh, R. C. A., Arrowsmith, C., Fleet, L., Triest, J., Sime, L.

621   C., Alemany, O., and Foord, S.: Recent Antarctic Peninsula warming relative to Holocene

622   climate and ice-shelf history, Nature, 489, 141–144, https://doi.org/10.1038/nature11391,

623   2012.

624   Ó Cofaigh, C., Davies, B. J., Livingstone, S. J., Smith, J. A., Johnson, J. S., Hocking, E. P.,

625   Hodgson, D. A., Anderson, J. B., Bentley, M. J., Canals, M., Domack, E., Dowdeswell, J.

626   A., Evans, J., Glasser, N. F., Hillenbrand, C.-D., Larter, R. D., Roberts, S. J., and Simms, A.

627   R.: Reconstruction of ice-sheet changes in the Antarctic Peninsula since the Last Glacial

628   Maximum, Quat Sci Rev, 100, 87–110,

629   https://doi.org/https://doi.org/10.1016/j.quascirev.2014.06.023, 2014.

630   Pedley, M., Paren, J. G., and Potter, J. R.: Localized Basal Freezing Within George VI Ice Shelf,

631   Antarctica, Journal of Glaciology, 34, 71–77, https://doi.org/DOI:

632   10.3189/S0022143000009084, 1988.

633   Pritchard, H. D., Arthern, R. J., Vaughan, D. G., and Edwards, L. A.: Extensive dynamic

634   thinning on the margins of the Greenland and Antarctic ice sheets, Nature, 461, 971–975,

635   https://doi.org/10.1038/nature08471, 2009.

636   Pritchard, H. D., Ligtenberg, S. R. M., Fricker, H. A., Vaughan, D. G., Van den Broeke, M. R.,

637   and Padman, L.: Antarctic ice-sheet loss driven by basal melting of ice shelves, Nature, 484,

638   502–505, 2012.

639   Rignot, E., Jacobs, S., Mouginot, J., and Scheuchl, B.: Ice-Shelf Melting Around Antarctica,

640   Science (1979), 341, 266–270, https://doi.org/10.1126/science.1235798, 2013.

641   Rignot, E., Mouginot, J., Scheuchl, B., van den Broeke, M., van Wessem, M. J., and Morlighem,

642   M.: Four decades of Antarctic Ice Sheet mass balance from 1979–2017, Proceedings of the

643   National Academy of Sciences, 201812883, https://doi.org/10.1073/pnas.1812883116,

644   2019.

645   Rignot, E., Mouginot, J., Scheuchl, B., and Jeong, S.: Changes in Antarctic Ice Sheet Motion

646   Derived From Satellite Radar Interferometry Between 1995 and 2022, Geophys Res Lett,

647   49, e2022GL100141, https://doi.org/https://doi.org/10.1029/2022GL100141, 2022.

648   Scambos, T., Fricker, H. A., Liu, C.-C., Bohlander, J., Fastook, J., Sargent, A., Massom, R., and

649   Wu, A.-M.: Ice shelf disintegration by plate bending and hydro-fracture: Satellite

650   observations and model results of the 2008 Wilkins ice shelf break-ups, Earth Planet Sci

651   Lett, 280, 51–60, https://doi.org/10.1016/j.epsl.2008.12.027, 2009.

652   Schannwell, C., Cornford, S., Pollard, D., and Barrand, N. E.: Dynamic response of Antarctic

653   Peninsula Ice Sheet to potential collapse of Larsen C and George VI ice shelves,

654   Cryosphere, 12, 2307–2326, https://doi.org/10.5194/tc-12-2307-2018, 2018.

655   Schoof, C.: Marine ice-sheet dynamics. Part 1. The case of rapid sliding, J Fluid Mech, 573, 27–

656   55, https://doi.org/10.1017/S0022112006003570, 2007.

657   Shepherd, A., Ivins, E. R., A, G., Barletta, V. R., Bentley, M. J., Bettadpur, S., Briggs, K. H.,

658   Bromwich, D. H., Forsberg, R., Galin, N., Horwath, M., Jacobs, S., Joughin, I., King, M.

659   A., Lenaerts, J. T. M., Li, J., Ligtenberg, S. R. M., Luckman, A., Luthcke, S. B., McMillan,

660   M., Meister, R., Milne, G., Mouginot, J., Muir, A., Nicolas, J. P., Paden, J., Payne, A. J.,

661   Pritchard, H., Rignot, E., Rott, H., Sørensen, L. S., Scambos, T. A., Scheuchl, B., Schrama,

662   E. J. O., Smith, B., Sundal, A. V, van Angelen, J. H., van de Berg, W. J., van den Broeke,

663   M. R., Vaughan, D. G., Velicogna, I., Wahr, J., Whitehouse, P. L., Wingham, D. J., Yi, D.,

664   Young, D., and Zwally, H. J.: A Reconciled Estimate of Ice-Sheet Mass Balance, Science

665   (1979), 338, 1183–1189, https://doi.org/10.1126/science.1228102, 2012.

666 Shevenell, A. E., Ingalls, A. E., Domack, E. W., and Kelly, C.: Holocene Southern Ocean

667   surface temperature variability west of the Antarctic Peninsula, Nature, 470, 250–254,

668   https://doi.org/10.1038/nature09751, 2011.

669 Smith, B., Fricker, H. A., Gardner, A. S., Medley, B., Nilsson, J., Paolo, F. S., Holschuh, N.,

670   Adusumilli, S., Brunt, K., Csatho, B., Harbeck, K., Markus, T., Neumann, T., Siegfried, M.

671   R., and Zwally, H. J.: Pervasive ice sheet mass loss reflects competing ocean and

672   atmosphere processes, Science (1979), eaaz5845, https://doi.org/10.1126/science.aaz5845,

673   2020.

674 Smith, J. A., Bentley, M. J., Hodgson, D. A., Roberts, S. J., Leng, M. J., Lloyd, J. M., Barrett, M.

675   S., Bryant, C., and Sugden, D. E.: Oceanic and atmospheric forcing of early Holocene ice

676   shelf retreat, George VI Ice Shelf, Antarctica Peninsula, Quat Sci Rev, 26, 500–516,

677   https://doi.org/https://doi.org/10.1016/j.quascirev.2006.05.006, 2007.

678 Sugden, D. E. and Clapperton, C. M.: An Ice-shelf Moraine, George VI Sound, Antarctica, Ann

679   Glaciol, 2, 135–141, https://doi.org/DOI: 10.3189/172756481794352298, 1981.

680 Wallis, B. J., Hogg, A. E., van Wessem, J. M., Davison, B. J., and van den Broeke, M. R.:

681   Widespread seasonal speed-up of west Antarctic Peninsula glaciers from 2014 to 2021, Nat

682   Geosci, https://doi.org/10.1038/s41561-023-01131-4, 2023.

683 Weertman, J.: On the sliding of glaciers, J. Glaciol., 3, 33–38, 1957.

684 Weertman, J. and Weertman, J.: Stability of the Junction of an Ice Sheet and an Ice Shelf,

685   Journal of Glaciology, 13, 3–11, https://doi.org/10.1017/S0022143000023327, 1974.

686